Rare earth Tb doped $Ni_{0.1}Cu_{0.1}Zn_{0.8}Fe_2O_4$ spinel ferrite@rGO composite: a novel catalyst for the removal of dyes, pesticides and drugs from industrial wastewater

I. Shakir [a], K. M. Katubi [b], S. Khalil [c], I. Boukhris [d], M. Anwar [c], A. Jabeen [c], M. S. Al-Buriahi [e], M. F. Warsi [c], M. I. Din [f, *]

[a] *Department of Physics, Faculty of Science, Islamic University of Madinah, Madinah 42351, Saudi Arabia*

[b] *Department of Chemistry, College of Science, Princess Nourah bint Abdulrahman University, P.O. Box 84428, Riyadh 11671, Saudi Arabia*

[c] *Institute of Chemistry, Baghdad-ul-Jadeed Campus, The Islamia University of Bahawalpur, Pakistan*

[d] *Department of Physics, Faculty of Science, King Khalid University; P.O. Box 9004, Abha; Saudi Arabia*

[e] *Department of Physics, Sakarya University, Sakarya, Turkey*

[f] *School of Chemistry University of the Punjab, Lahore 54590, Pakistan*

This study present synthesis of spinel ferrites ($ZnFe_2O_4$, $Ni_{0.1}Cu_{0.1}Zn_{0.8}Fe_2O_4$, Tb-$Ni_{0.1}Cu_{0.1}Zn_{0.8}Fe_2O_4$) by co-precipitation and its composite Tb- $Ni_{0.1}Cu_{0.1}Zn_{0.8}Fe_2O_4$@rGO by ultrasonication means. The bandgap was found in the range 1.67-2.05 eV. Under optimal conditions, Tb- $Ni_{0.1}Cu_{0.1}Zn_{0.8}Fe_2O_4$/rGO was seen to degrade methyl orange, pendimethalin, and ofloxacin at rates of 83%, 69.50%, and 50.37%, under visible light. The mechanism was elucidated by scavenger studies, which demonstrated that the primary reactive radicals driving the degradation process were superoxide radicals (O_2*$^-$) and hydroxyl radicals (OH*). The remarkable rate constant of MO dye degradation demonstrated by Tb-$Ni_{0.1}Cu_{0.1}Zn_{0.8}Fe_2O_4$/rGO was 0.0339 min^{-1}, whereas $ZnFe_2O_4$ showed 0.0088 min^{-1}.

(Received April 11, 2025; Accepted July 15, 2025)

Keywords: Rare earth, Spinel ferrites, XRD, Photocatalysis, Wastewater

1. Introduction

Industrial growth and the rapid depletion of fossil fuels have led to major global concerns such as surface water pollution, a contaminated environment, energy shortage, and the availability of clean water [1]. A wide range of industrial and anthropogenic human endeavors, such as agricultural, textile, metallurgy, leather, steel, and pharmaceutical [2] discharging their raw hazardous wastes into the environment as chemical pollutants. These hazardous contaminants, which are potentially dangerous, carcinogenic, and non-biodegradable, either float on the surface of water bodies or dissolve in them degrading the environment [3]. Scientists have developed various techniques for removing toxic pollutants from wastewater, including chemical precipitation, adsorption and coagulation etc. However, the effectiveness and wide-scale application of these techniques are limited, due to factors such as removal efficiency, operational complexity, and the formation of pathogenic and cancerous intermediates. Advanced oxidation-based techniques particularly photocatalysis, offer a range of applications in wastewater treatment due to their design flexibility, quick reaction times, and high degradation efficiency [4].

For many years, research has been conducted on the degradation of pollutants using metal oxides, and their hybrid nanostructures. The drawbacks of conventional photocatalysts include low absorption, photo-corrosion, a broad bandwidth, and a higher rate of electron-hole recombination. These includes for instance TiO_2 [5], ZnO [6] γ-Fe_2O_3/ZnO [7], CeO_2/g-C_3N_4 [8], SnO_2 [9], CuO/ZnO [10], and Fe_3O_4/ZnO. Among these, the optical, electrical, and magnetic properties of

* Corresponding author: imrandin2007@gmail.com
https://doi.org/10.15251/DJNB.2025.203.793

spinel ferrite are attributed to the tetrahedral sites occupied by M^{2+} ions (e.g., Zn^{2+}, Co^{2+}, Cu^{2+}, Ni^{2+} etc.) and the octahedral sites by Fe^{3+} ions. Zinc ferrite nanoparticles have been of significant interest due to their usefulness in several magnetic applications. The structure of zinc ferrite allows for great photocatalytic abilities and the production of hydrogen from water using light. Multiple studies reported in the literature have revealed that $ZnFe_2O_4$ has a bandgap of 1.9 eV and less toxic. This outstanding characteristic makes it exceptionally well-suited for a wide range of photocatalytic applications. However, its antiferromagnetic property restrict its potential for recovery and reuse. Doping Zn^{2+} sites with rare earth cations like Nd^{3+}, Tb^{3+}, Dy^{3+}, Sm^{3+} and Tm^{3+} can enhance the performance of ferrite. These ions can change the behavior of ferrite from antiferromagnetic to ferromagnetic [11]. The difference in size between Fe^{3+} ions induce a deformation in the spinel structure of ferrite, thereby greatly amplifying the properties of nanomaterials [12]. The 4f electrons in rare earth elements are screened by outer $5s^25p^6$ sub-shells, causing strong spin-orbit angular momentum coupling [13]. The coupling of spinel crystal structure impacts its electronic state, Fe_2O_3 complicates the synthesis of Tb-substituted NiCuZn ferrite, and the inclusion of Tb^{3+} ions, significantly modifies the magnet anisotropy of the system [14].

Rare-earth doped NiCuZn ferrites have good electromagnetic propertie. However, high bulk density limits their application. Numerous studies have been conducted to improve the photocatalytic efficiency and energy storage capabilities of $NiCuZnFe_2O_4$. These studies include $S/gCN\text{-}Ni_xCu_{1-x}Fe_2O_4$ [15], $NiZnFe_2O_4/g\text{-}CN$ [16], $Ni/ZnFe_2O_4$ [17], $Dy/ZnMgFe_2O_4$ [18], $NiCuZnFe_2O_4$ [19] and many more. Based on Patil *et al*.'s work, raising the La^{3+} ion concentration in NiCuZn ferrites caused a significant decrease in saturation magnetization and magnetic moment [20]. A thorough investigation into the impact of Tb^{3+} substitution on the optical, magnetic, and structural characteristics of $NiCuZnFe_2O_4$ was carried out by Vidyadhar Awati *et al*.[21]. Almessiere *et al*., studied the properties of Tb-doped NiCuZn [22]. Raees M. Asif and his colleagues recently presented a remarkable study on a dual-band MIMO antenna's performance. The antenna was designed with a Tb-doped Ni-Zn ferrite substrate, specifically tailored for cutting-edge 5G applications [23]. Through the sol-gel auto-combustion method, Jamdade *et al.* conducted a comprehensive analysis of the magnetic and structural properties of Tb^{3+} doped $ZnFe_2O_4$ [24].

Heterojunction arrangements containing semiconductor composites greatly improve ferrite performance [25]. The extraordinary properties of graphene-based materials, such as their great stability, remarkable strength, fast adsorption rate, and phenomenal surface area, have been the subject of extensive investigation [26]. In addition to having superior electrical conductivity, rGO is more effective at adsorbing organic pollutants via the p-p bond [27]. CuO/CdFe@rGO ternary composites exhibit exceptional photocatalytic performance, as reported by Amna *et al.*, because of the rGO sheets' large surface area and increased number of active sites [28]. Beriham Basha *et al.* used a highly efficient wet chemical approach to synthesize a nanocomposite Cr-doped $CoFe_2O_4$@rGO. Benzoic acid and rhodamine B were to be degrade by photodegradation [29].

Considering all the previously described approaches, we have fabricated $ZnFe_2O_4$, $Ni_{0.1}Cu_{0.1}Zn_{0.8}Fe_2O_4$, Tb doped $Ni_{0.1}Cu_{0.1}Zn_{0.8}Fe_2O_4$ photocatalysts through a co-precipitation process and a composite with rGO (Tb- $Ni_{0.1}Cu_{0.1}Zn_{0.8}Fe_2O_4$/rGO) via ultra-sonication technique to degrade organic contaminants. By trapping the species of charge carriers and reducing charge recombination, the rGO sheets in the composite sample and doping work together to control the band gap and enhance the composite's photocatalytic activity. Methyl orange, pendimethalin, and ofloxacin were among the specific contaminants that the as-synthesized catalysts were used to photodegrade utilizing a probe reaction. To minimize any potential adverse impacts on human health and the environment, this study intends to achieve two significant objectives: (1) developing a simple method to fabricate nanostructure photocatalysts using $ZnFe_2O_4$, $Ni_{0.1}Cu_{0.1}Zn_{0.8}Fe_2O_4$, Tb-$Ni_{0.1}Cu_{0.1}Zn_{0.8}Fe_2O_4$, Tb- $Ni_{0.1}Cu_{0.1}Zn_{0.8}Fe_2O_4$ /rGO and (2) using these photocatalysts to efficiently treat both established and newly emerging pollutants in wastewater.

2. Experimental

2.1. Chemicals

Analytical-grade chemicals were acquired from Sigma Aldrich as follow: copper nitrate (Cu $(NO_3)_2.6H_2O$), rare earth element terbium nitrate (Tb $(NO_3)_3.5H_2O$), ferric nitrate nonahydrate (Fe $(NO_3)_3.9H_2O$), powdered Graphite (99%), zinc nitrate (Zn $(NO_3)_2.6H_2O$), sulphuric acid (H_2SO_4), nickel nitrate (Ni $(NO_3)_2.6H_2O$),Potassium permanganate ($KMnO_4$), Sodium nitrate ($NaNO_3$), Hydrogen peroxide (H_2O_2), hydrazine ($N_2H_4{\cdot}H_2O$), aqueous ammonia (NH_3 (aq.)), deionized water, methyl orange dye, pendimethalein, and ofloxacin.

2.2. Synthesis of graphene oxide

Graphene oxide (GO) was synthesized using the Hummers method with 3g graphite and 3g $NaNO_3$ combined with conc. H_2SO_4 . The mixture was agitated in an ice bath for 35 minutes, adding $KMnO_4$ to turn it greenish. A purple-brown slurry was synthesized after stirring for 48 hours, and washed with deionized water and hydrogen peroxide. When the reducing agent H_2O_2 is added, $KMnO_4$ transformed into soluble $MnSO_4$, resulting in a yellow suspension. Four times, the thick yellow residue was washed with a solution of 1 W% H_2SO_4 and 1 W% H_2O_2 to remove nonreactive metal ions. The yellow residue was finally cleaned off with deionized water to produce a graphene oxide paste that was dark brown in color [30].

2.3. Reduction of graphene oxide

Reduced graphene oxide (rGO) was synthesized by reducing the graphene solution (Fig. 1). This method produced a black, uniform slurry when 30 ml of graphene oxide was diluted with distilled water and ultrasonicated for two hours. A reducing chemical called hydrazine (N_2H_4) hydrate converts graphene oxide into black reduced graphene oxide, and 0.3 mL ammonia were added to graphene oxide sheets to exfoliate them. The mixture was stirred at 90°C for 1.5 hours using a paraffin oil bath. At 80°C, it was oven-dried [31].

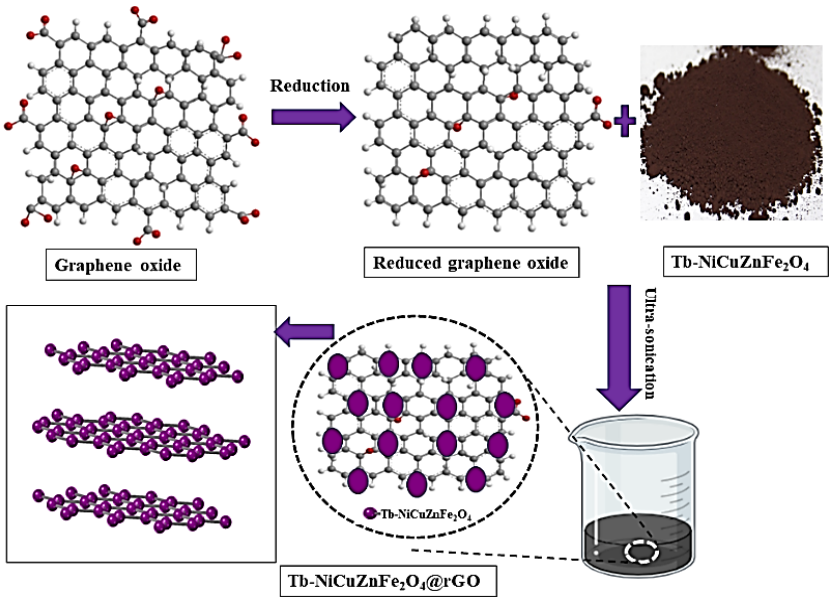

Fig 1. Schematic illustration of reduction of graphene oxide and attachment of Tb- $Ni_{0.1}Cu_{0.1}Zn_{0.8}Fe_2O_4$ nanoparticles.

2.4. Synthesis of nickel copper zinc ferrite ($Ni_{0.1}Cu_{0.1}Zn_{0.8}Fe_2O_4$)

$Ni_{0.1}Cu_{0.1}Zn_{0.8}Fe_2O_4$ was fabricated via chemical co-precipitation. To begin with, precisely 24.2 g Fe $(NO_3)_3.9H_2O$, 0.58 g Ni $(NO_3)_2.6H_2O$, 0.59 g Cu $(NO_3)_2.6H_2O$, and 7.43 g Zn $(NO_3)_2.6H_2O$ were added to 400 mL of deionized water in four different beakers, respectively. After that, each mixture was stirred for 30 minutes to obtain a thoroughly combined and consistent solution. Until the pH reaches 12, 0.2 M NaOH is added dropwise while being continuously stirred. Precipitates formed at 70°C after stirring for 30–40 min and then sonicated for 30 minutes. After many washes, the precipitates were dried at 120°C. Sample was then calcined for three hours at 500°C.

2.5. Synthesis of terbium doped nickel copper zinc ferrite nanoparticles

Using the co-precipitation method, Tb doped $Ni_{0.1}Cu_{0.1}Zn_{0.8}Fe_2O_4$ nanoparticles were synthesized (Fig. 2). The following precise amounts were added to each beaker: zinc nitrate (7.43 g), ferric nitrate nonahydrate (24.2 g), copper nitrate (0.59 g), and nickel nitrate (0.58 g). After that, each mixture was stirred for 30 minutes. Next, the combined solutions and 10 mL of terbium nitrate (Tb $(NO_3)_3.5H_2O$) must be vigorously stirred. 0.2 M NaOH is added drop by drop while swirling constantly to bring the pH up to 12. Precipitates formed at 70 °C after stirring for 30 to 40 minutes. The precipitates were sonicated, oven-dried, and calcinated for three hours to produce nanoparticles.

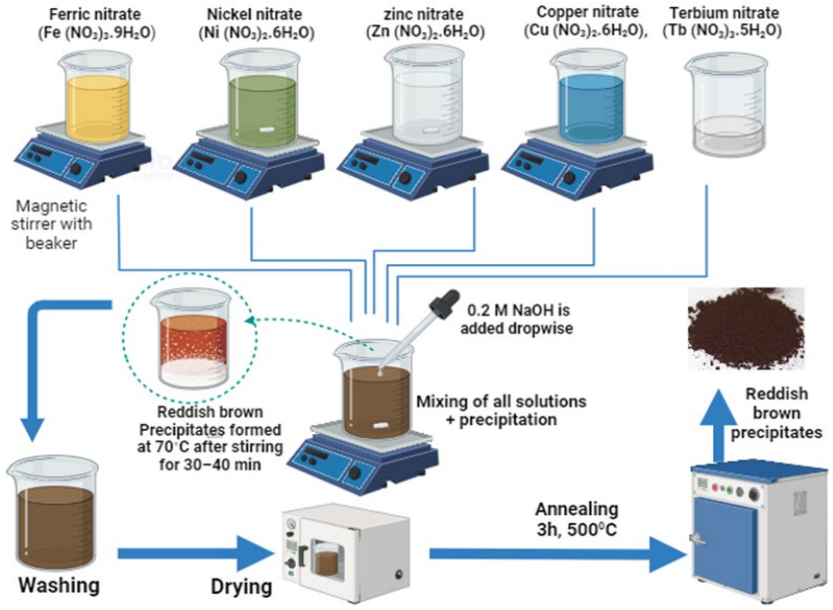

Fig. 2. Schematic illustration for the synthesis of $Ni_{0.1}Cu_{0.1}Zn_{0.8}Fe_2O_4$ nanoparticles.

2.6. Synthesis of Tb doped $NiCuZnFe_2O_4$@rGO nanocomposite

$Ni_{0.1}Cu_{0.1}Zn_{0.8}Fe_2O_4$-based nanocomposite with Tb doping and composite with rGO was synthesized via the ultrasonication method. To fabricate the composite, 240 mg of Tb-doped $Ni_{0.1}Cu_{0.1}Zn_{0.8}Fe_2O_4$ and 80 mg of rGO powder were mixed with 50 mL of distilled water. The mixture was then subjected to ultra-sonication until it became homogeneous. The resulting composite was dried at 120 °C and characterized using various techniques (Fig. 1).

2.7. Characterization of photocatalyst

The phase analysis and crystal structure of the fabricated photocatalysts were investigated with an Xpert PRO 30-40-60 diffractometer. Within the 2θ range of 20-80°, Cu-Kα radiations were utilized. We used the Scherer formula and the XRD data analysis to get the average crystal size of Zn ferrite samples. An Agilent dual-beam Ultraviolet-Visible spectrometer was utilized to perform a thorough examination of the bandgap and photocatalytic characteristics. Using Tauc's standard relation, the band gap energy (E_g) was found.

$$\alpha h\nu = A\,(h\nu - E_g)^{1/2} \quad (1)$$

where the optical band gap energy is represented by E_g, the material's absorption coefficient is indicated by α, and the relevant photon energy is indicated by hν.

2.8. Photocatalytic experiment

$ZnFe_2O_4$, $Ni_{0.1}Cu_{0.1}Zn_{0.8}Fe_2O_4$, Tb- $Ni_{0.1}Cu_{0.1}Zn_{0.8}Fe_2O_4$, photocatalysts were used as testing models under tungsten lamp (300 W) to determine their photocatalytic efficiency in relation to Tb-$Ni_{0.1}Cu_{0.1}Zn_{0.8}Fe_2O_4$ /rGO nanocomposites for the degradation of methyl orange, pendimethalin, and ofloxacin, respectively. To carry out the degradation process, three solutions were prepared: a dye (30 ppm), drug (30 ppm), and pesticidesolution (1 ppm). As prepared catalyst was utilized in a 5 mgL^{-1} solution of each pollutant in distilled water to assess the degradation of organic pollutants. To measure the absorbance spectrum, repeat the preceding step for 50 minutes while stirring continuously. The percentage degradation (2), rate constant (3) and half-life (4) were computed using the following mathematical formulas.

$$\% \text{ degradation} = \frac{1 - C_t}{C_o} \times 100 \tag{2}$$

$$-ln\frac{A_t}{A_o} = Kt \tag{3}$$

$$t_{1/2} = \frac{0.693}{K} \tag{4}$$

2.9. Active substance analysis

The active species capture analysis was performed using Tb- $Ni_{0.1}Cu_{0.1}Zn_{0.8}Fe_2O_4$/rGO, and the photocatalytic degradation of MO dye was investigated. The electrons (e^-), hydroxyl radicals (OH*), holes (h^+) and superoxide radicals (O_2^{*-}) were scavenged using a variety of trapping agents, including $AgNO_3$, 2-propanol, EDTA and ascorbic acid respectively.

3. Results and discussion

3.1. Structural investigation and phase analysis

The compared to FP and CC plans was calculated. Using the X-ray diffraction (XRD) technique, the structure of the fabricated photocatalyst was examined. Fig. 3 depicts the XRD patterns of fabricated photocatalyst i.e. $ZnFe_2O_4$, $Ni_{0.1}Cu_{0.1}Zn_{0.8}Fe_2O_4$, Tb- $Ni_{0.1}Cu_{0.1}Zn_{0.8}Fe_2O_4$, and Tb- $Ni_{0.1}Cu_{0.1}Zn_{0.8}Fe_2O_4$ /rGO. The specific diffraction angles of fabricated photocatalyst at 18.11°, 29.77 °, 35.20 °, 36.73 °, 42.95 °, 53.67 °, and 56.98 ° that are associated with Millar indices of an Fd3m spinel crystal structure as (111), (220), (311), (222), (400), (422), and (511) respectively (JCPDS 00-022-1012) [32]. One extra diffraction peak appeared at 43.93 ° which is highlighted as * in the XRD pattern is due to the sample holder. The XRD analysis indicate that the fabricated photocatalyst exhibit cubic spinel structures, whereby Fe^{+3} ions occupy octahedral positions and Zn^{+2} ions occupy tetrahedral sites. The characteristic peak of the cubic phase of $ZnFe_2O_4$ is responsible for the noticeable peak located in the (311) plane at 35.20◦. Doping in the bare sample resulted in intensity transition and peak shift, as Fig. 3b demonstrates quite well. A moderate peak strength in the fabricated ferrite samples indicates a low degree of crystallinity, and peaks broadening indicates the nanoscale size of the crystallite. Even in rare-earth doped ferrites at low doping concentrations, several researchers have reported the production of the orthorhombic phase ($TbFeO_3$). Some minor peaks were observed in $ZnFe_2O_4$ at diffraction angles 33° and 50.3° corresponding to Fe_2O_3 [JCPDS No-33-0664].

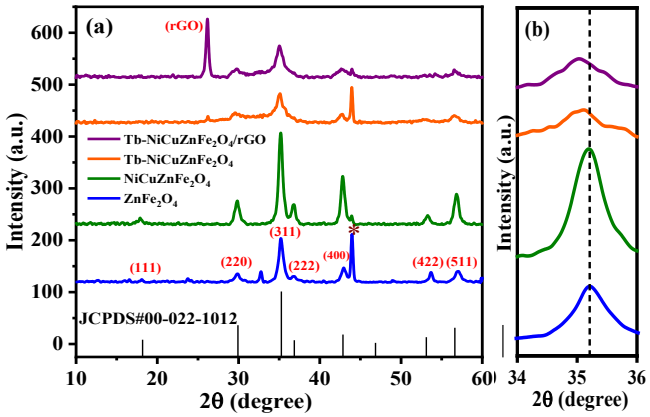

Fig. 3. Phase analysis of fabricated photocatalysts (a) $ZnFe_2O_4$, (b) $Ni_{0.1}Cu_{0.1}Zn_{0.8}Fe_2O_4$ (c) Tb-$Ni_{0.1}Cu_{0.1}Zn_{0.8}Fe_2O_4$ and (d) Tb- $Ni_{0.1}Cu_{0.1}Zn_{0.8}Fe_2O_4$ /rGO.

Additionally, a number of crystallographic characteristics about the synthesized samples were computed and are listed in Table 1. By using the Debye-Scherrer formula the crystallite size (D) of $ZnFe_2O_4$, $Ni_{0.1}Cu_{0.1}Zn_{0.8}Fe_2O_4$, Tb- $Ni_{0.1}Cu_{0.1}Zn_{0.8}Fe_2O_4$, and Tb- $Ni_{0.1}Cu_{0.1}Zn_{0.8}Fe_2O_4$ /rGO nanoparticles was determined [33].

$ZnFe_2O_4$, $Ni_{0.1}Cu_{0.1}Zn_{0.8}Fe_2O_4$, Tb- $Ni_{0.1}Cu_{0.1}Zn_{0.8}Fe_2O_4$, and Tb- $Ni_{0.1}Cu_{0.1}Zn_{0.8}Fe_2O_4$/rGO crystallite sizes were 11.7, 12, 16.9, and 14 nm, respectively. Additionally, the dislocation density was computed using the provided formula. The size of crystallites and the density of dislocations have inverse connections. The decrease in crystallite size can be attributed to a high dislocation density.

$$\text{Dislocation Density} = \frac{1}{D^2} \tag{5}$$

Table.1 XRD findings of $ZnFe_2O_4$, $Ni_{0.1}Cu_{0.1}Zn_{0.8}Fe_2O_4$, Tb- $Ni_{0.1}Cu_{0.1}Zn_{0.8}Fe_2O_4$ and Tb-$Ni_{0.1}Cu_{0.1}Zn_{0.8}Fe_2O_4$ /rGO.

Material	$ZnFe_2O_4$	$Ni_{0.1}Cu_{0.1}Zn_{0.8}Fe_2O_4$	Tb-$Ni_{0.1}Cu_{0.1}Zn_{0.8}Fe_2O_4$	Tb-$Ni_{0.1}Cu_{0.1}Zn_{0.8}Fe_2O_4$ /rGO
Geometry	Cubic	Cubic	Cubic	Cubic
Crystallite Size (nm)	11.68	12.07	16.98	14.03
Dislocation Density	73.24	68.55	34.66	50.74
d-spacing (nm)	0.2545	0.2548	0.2557	0.2554
FWHM (β)	0.648	0.627	0.446	0.5396

3.2. Investigation of bandgap energies and optical properties

UV-Vis spectra of $ZnFe_2O_4$, $Ni_{0.1}Cu_{0.1}Zn_{0.8}Fe_2O_4$, Tb-$Ni_{0.1}Cu_{0.1}Zn_{0.8}Fe_2O_4$, and Tb-$Ni_{0.1}Cu_{0.1}Zn_{0.8}Fe_2O_4$/rGO composite were displayed in Fig. 4 to investigate the excitation behavior. Within the wavelength range of about 200–800 nm, the absorption spectra of the fabricated materials were recorded. These absorption spectra were also used to calculate the bandgap energy (E_g) of the fabricated materials. The absorption coefficient, the energy of photon, and proportionality constant are represented by the letters A, hυ, and α in the equation above. The Tauc curve can be extrapolated on the hv axis (x-intercept) to approximate the E_g value. Fig. 4, rGO displayed two characteristic absorption bands at 234 nm and 315 nm, which are induced by the π-π* (C=C) and n-π* (C=O) electronic transitions. The findings unmistakably demonstrate that graphene has a major effect on

optical characteristics of Tb-NiCuZnFe$_2$O$_4$, pointing to a potential enhancement of the compound's visible light-induced photo-catalytic response (Tb- Ni$_{0.1}$Cu$_{0.1}$Zn$_{0.8}$Fe$_2$O$_4$/rGO). The size and composition of a material determine its bandgap. ZnFe$_2$O$_4$, Ni$_{0.1}$Cu$_{0.1}$Zn$_{0.8}$Fe$_2$O$_4$, Tb-Ni$_{0.1}$Cu$_{0.1}$Zn$_{0.8}$Fe$_2$O$_4$, and Tb- Ni$_{0.1}$Cu$_{0.1}$Zn$_{0.8}$Fe$_2$O$_4$ /rGO nanoparticle catalysts have computed bandgaps of 2.05 eV, 2.01 eV, 1.82 eV, and 1.67 eV respectively (Fig. 5). By applying the Tauc relationship, the Eg value of the bare ZnFe$_2$O$_4$ sample was around 2.05 eV [34].

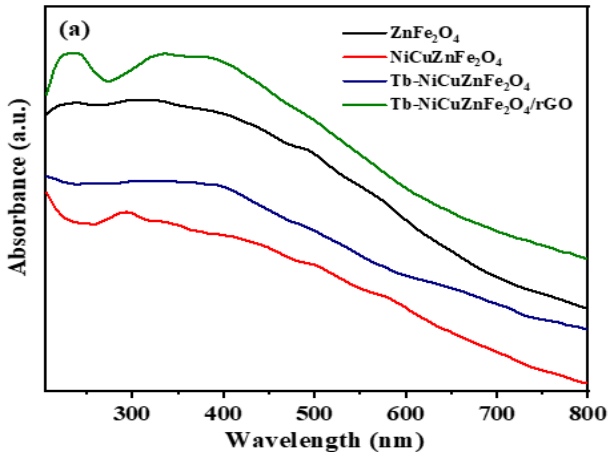

Fig. 4. Absorption spectra of fabricated photo-catalysts (a) ZnFe$_2$O$_4$, (b Ni$_{0.1}$Cu$_{0.1}$Zn$_{0.8}$Fe$_2$O$_4$ (c) Tb-Ni$_{0.1}$Cu$_{0.1}$Zn$_{0.8}$Fe$_2$O$_4$ and (d) Tb- Ni$_{0.1}$Cu$_{0.1}$Zn$_{0.8}$Fe$_2$O$_4$ /rGO.

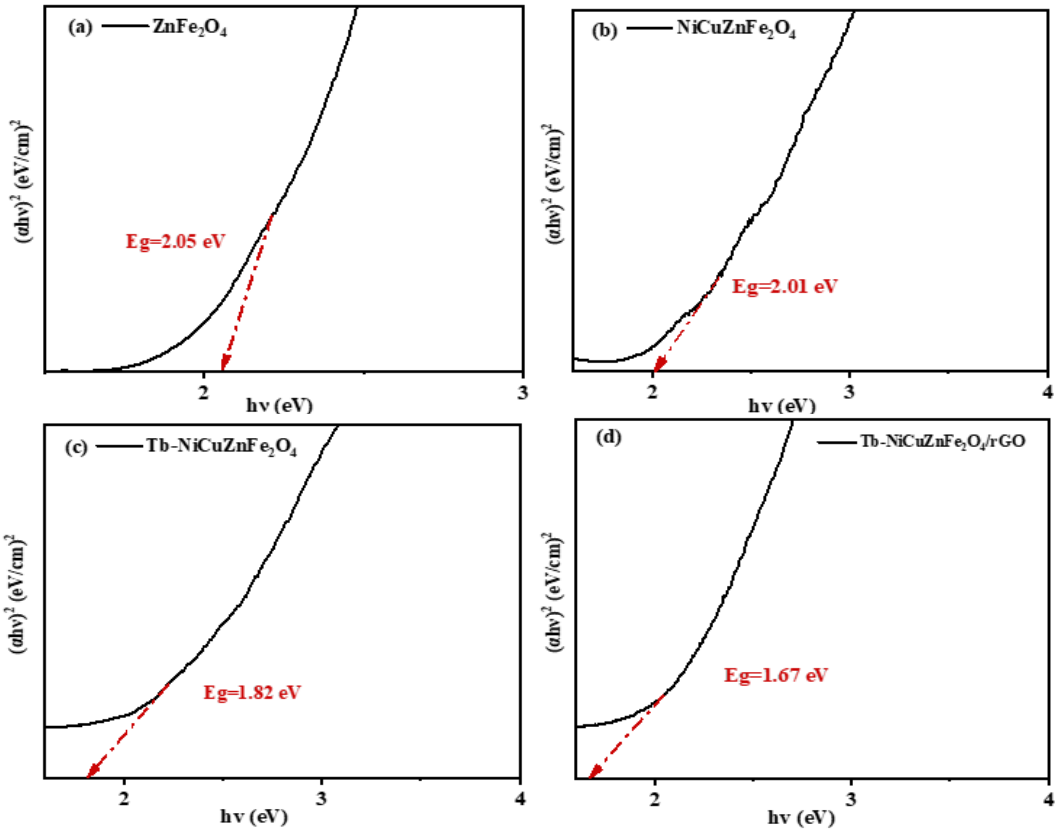

Fig. 5. Bandgap energies of fabricated photo-catalysts (a) ZnFe$_2$O$_4$, (b) Ni$_{0.1}$Cu$_{0.1}$Zn$_{0.8}$*Fe$_2$O$_4$ (c) Tb-*Ni$_{0.1}$Cu$_{0.1}$Zn$_{0.8}$*Fe$_2$O$_4$ and (d) Tb-* Ni$_{0.1}$Cu$_{0.1}$Zn$_{0.8}$*Fe$_2$O$_4$ /rGO.*

3.3. Measurements of photocatalytic degradation

$ZnFe_2O_4$, $Ni_{0.1}Cu_{0.1}Zn_{0.8}Fe_2O_4$, Tb- $Ni_{0.1}Cu_{0.1}Zn_{0.8}Fe_2O_4$, and Tb- $Ni_{0.1}Cu_{0.1}Zn_{0.8}Fe_2O_4$/rGO photocatalysts were used to observe the photocatalytic degradation of MO (Fig. 6). Results showed two distinct absorption bands, visible at 464 nm and UV at 272 nm, due to dye chromophore structure [35]. The absorption decreased over time which may be due to the disruption of the aromatic ring structure of methyl orange molecules. Each solution was assessed for absorbance ("A_t"), and five milliliters (mL) were taken every five minutes. Fig. 7(a, b) displays the kinetic graphs of the photocatalytic reactions. The rate constant (k) value was ascertained by applying the first-order rate equation. The rate constants for the $ZnFe_2O_4$, $Ni_{0.1}Cu_{0.1}Zn_{0.8}Fe_2O_4$, Tb-$Ni_{0.1}Cu_{0.1}Zn_{0.8}Fe_2O_4$, and Tb- $Ni_{0.1}Cu_{0.1}Zn_{0.8}Fe_2O_4$/rGO photocatalysts against methyl orange are displayed in Fig. 7d and are, respectively, 0.0088 min^{-1}, 0.0118 min^{-1}, 0.0274 min^{-1}, and 0.0339 min^{-1}. In comparison to other prepared catalysts, it indicates that Tb- $Ni_{0.1}Cu_{0.1}Zn_{0.8}Fe_2O_4$ /rGO photodegraded MO more quickly. The percentages of MO that are degraded by $ZnFe_2O_4$, $Ni_{0.1}Cu_{0.1}Zn_{0.8}Fe_2O_4$, Tb- $Ni_{0.1}Cu_{0.1}Zn_{0.8}Fe_2O_4$, and Tb- $Ni_{0.1}Cu_{0.1}Zn_{0.8}Fe_2O_4$/rGO are 38%, 46%, 78% and 83% respectively (Table 2).

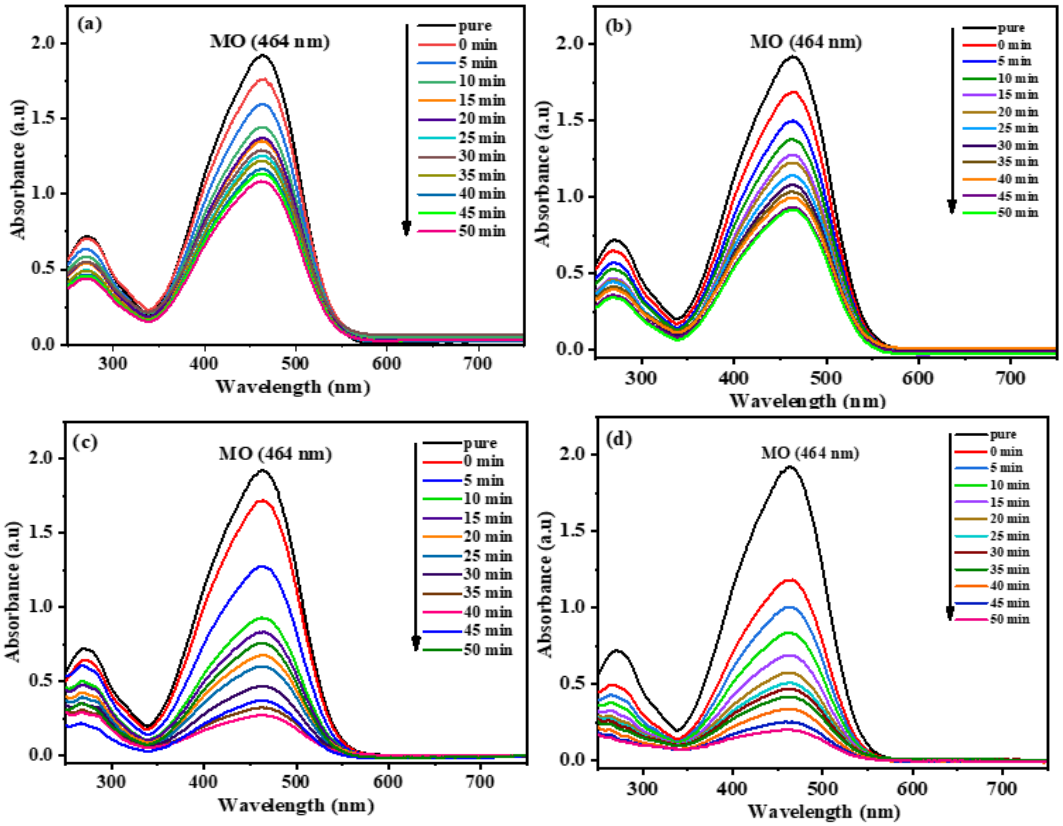

Fig. 6. At wavelength of 464 nm, the absorption spectra of MO (a) $ZnFe_2O_4$, (b) $Ni_{0.1}Cu_{0.1}Zn_{0.8}Fe_2O_4$ (c) Tb-$Ni_{0.1}Cu_{0.1}Zn_{0.8}Fe_2O_4$ and (d) Tb-$Ni_{0.1}Cu_{0.1}Zn_{0.8}Fe_2O_4$ /rGO nanocomposite.

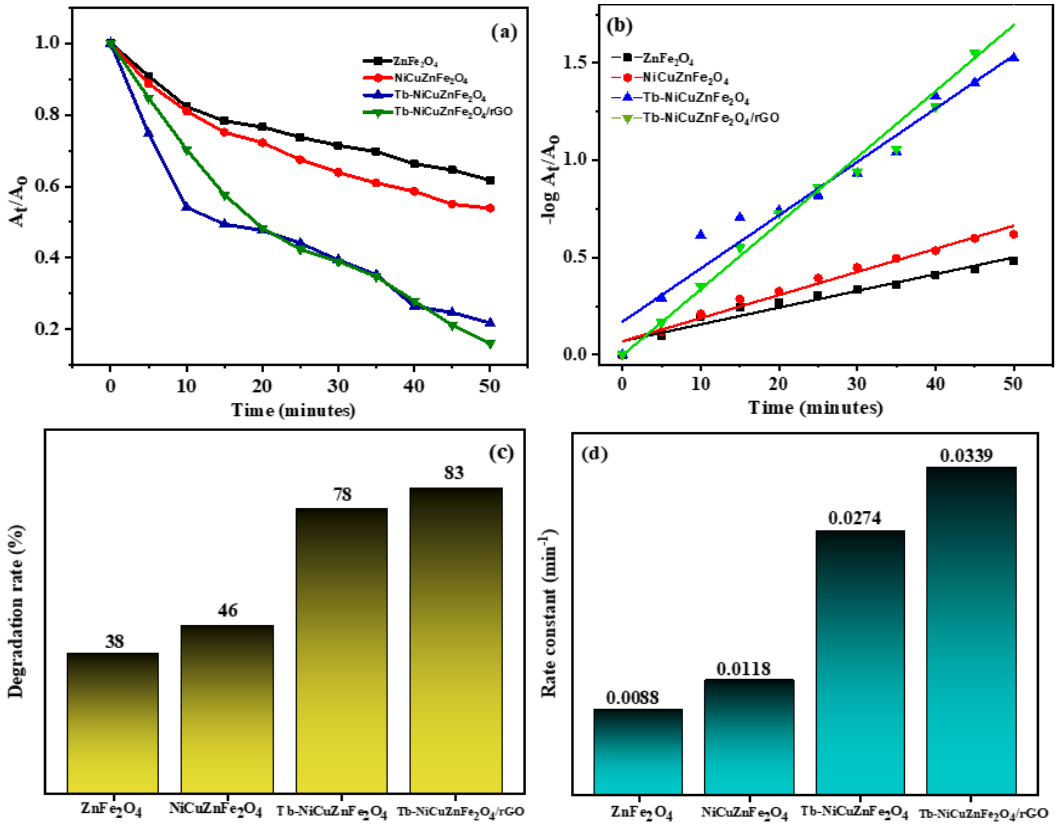

Fig. 7. (a, b) Kinetic graphs, (c) percentage degradation, and (d) rate constants of MO using $ZnFe_2O_4$, $Ni_{0.1}Cu_{0.1}Zn_{0.8}Fe_2O_4$, Tb- $Ni_{0.1}Cu_{0.1}Zn_{0.8}Fe_2O_4$ and Tb-$Ni_{0.1}Cu_{0.1}Zn_{0.8}Fe_2O_4$/rGO nanocomposites.

Table 2. Kinetic characteristics of the fabricated photocatalysts degradation of methyl orange.

Fabricated photocatalysts	$ZnFe_2O_4$	$Ni_{0.1}Cu_{0.1}Zn_{0.8}Fe_2O_4$	Tb-$Ni_{0.1}Cu_{0.1}Zn_{0.8}Fe_2O_4$	Tb-$Ni_{0.1}Cu_{0.1}Zn_{0.8}Fe_2O_4$ /rGO
% Degradation	38	46	78	83
Rate constant(min^{-1})	0.0088	0.0118	0.0274	0.0339
R^2	0.9500	0.9732	0.9577	0.984
Adj. R^2	0.9444	0.9703	0.9530	0.9822
Half life	78.75	58.72	25.29	20.44

The photocatalytic degradation of ofloxacin was evaluated by using $ZnFe_2O_4$, $Ni_{0.1}Cu_{0.1}Zn_{0.8}Fe_2O_4$, Tb- $Ni_{0.1}Cu_{0.1}Zn_{0.8}Fe_2O_4$, and Tb- $Ni_{0.1}Cu_{0.1}Zn_{0.8}Fe_2O_4$/rGO photocatalysts Fig. 8. The rate constant (k) was determined using the first-order rate equation. $ZnFe_2O_4$, $Ni_{0.1}Cu_{0.1}Zn_{0.8}Fe_2O_4$, Tb- $Ni_{0.1}Cu_{0.1}Zn_{0.8}Fe_2O_4$, and Tb- $Ni_{0.1}Cu_{0.1}Zn_{0.8}Fe_2O_4$/rGO photocatalysts against ofloxacin have rate constants of 0.00198 min^{-1}, 0.00531 min^{-1}, 0.00897 min^{-1}, and 0.01129 min^{-1}, respectively, as shown in Fig. 9d and Table 3. This indicates that Tb- $Ni_{0.1}Cu_{0.1}Zn_{0.8}Fe_2O_4$/rGO photodegraded ofloxacin more quickly than other synthesized photocatalysts. Figure 9c displays the % removal of ofloxacin by each of the four fabricated photocatalysts. The % degradation of ofloxacin by $ZnFe_2O_4$, $Ni_{0.1}Cu_{0.1}Zn_{0.8}Fe_2O_4$, Tb- $Ni_{0.1}Cu_{0.1}Zn_{0.8}Fe_2O_4$, and Tb- $Ni_{0.1}Cu_{0.1}Zn_{0.8}Fe_2O_4$ /rGO is 12.73%, 28.08%, 40% and 50.37% respectively. With a 50.37% drug removal rate for ofloxacin in 50 minutes, it is evident that the Tb- $Ni_{0.1}Cu_{0.1}Zn_{0.8}Fe_2O_4$ /rGO exhibited good photodegradation ability.

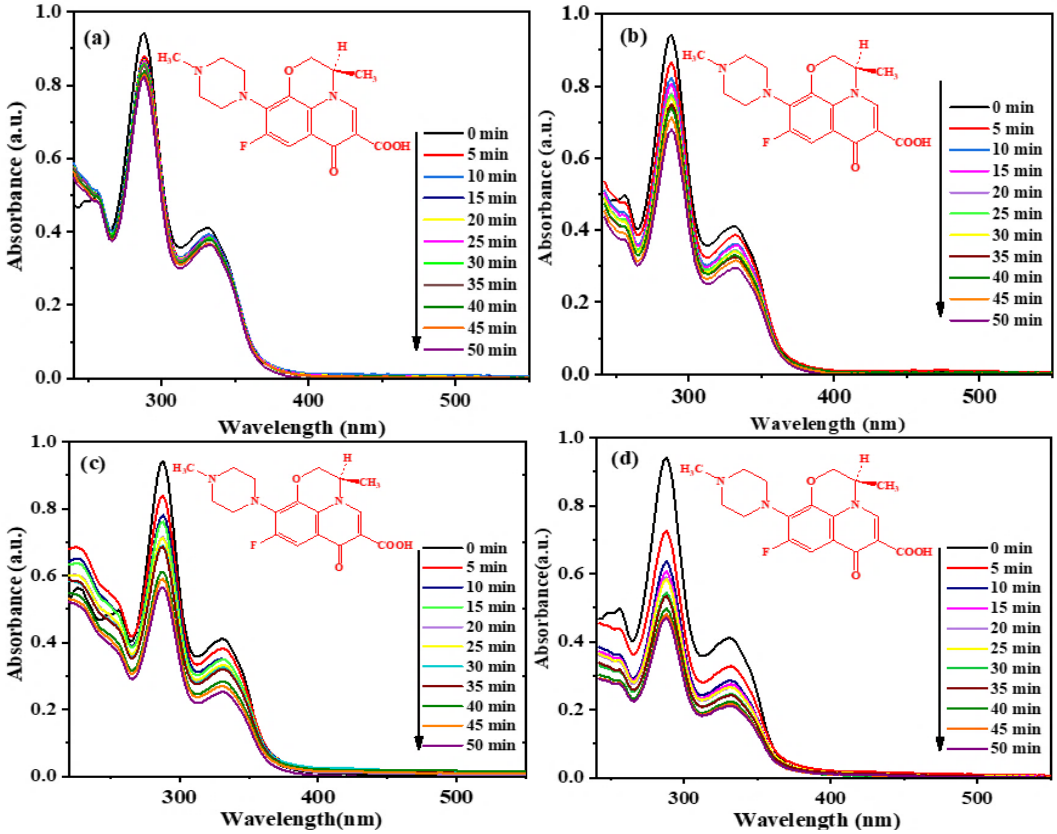

Fig. 8. The absorption spectra of Ofloxacin (a) $ZnFe_2O_4$, (b) $Ni_{0.1}Cu_{0.1}Zn_{0.8}Fe_2O_4$, (c) Tb-$Ni_{0.1}Cu_{0.1}Zn_{0.8}Fe_2O_4$, and (d) Tb- $Ni_{0.1}Cu_{0.1}Zn_{0.8}Fe_2O_4$ /rGO nanocomposite.

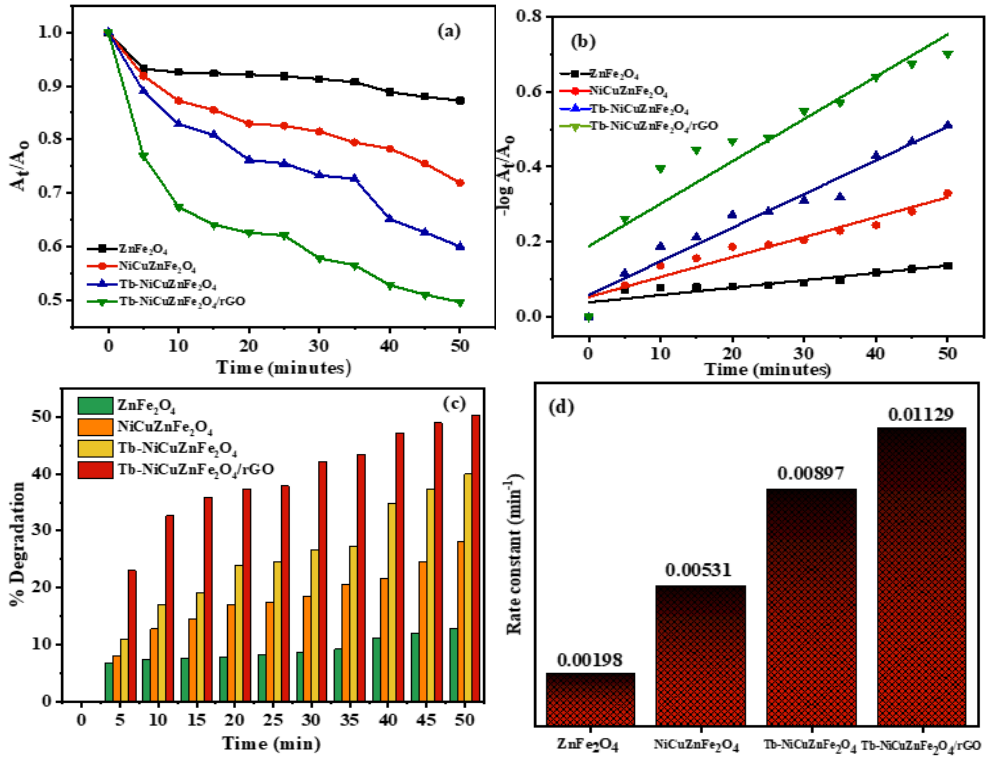

Fig. 9. (a, b) Kinetic graphs, (c) percentage degradation vs. time, and (d) rate constants of ofloxacin using $ZnFe_2O_4$, $Ni_{0.1}Cu_{0.1}Zn_{0.8}Fe_2O_4$, Tb- $Ni_{0.1}Cu_{0.1}Zn_{0.8}Fe_2O_4$ and Tb-$Ni_{0.1}Cu_{0.1}Zn_{0.8}Fe_2O_4$/rGO nanocomposites.

Table 3. Kinetic characteristics of the fabricated photocatalysts' degradation of Ofloxacin drug.

Sample	$ZnFe_2O_4$	$Ni_{0.1}Cu_{0.1}Zn_{0.8}Fe_2O_4$	Tb- $Ni_{0.1}Cu_{0.1}Zn_{0.8}Fe_2O_4$	Tb- $Ni_{0.1}Cu_{0.1}Zn_{0.8}Fe_2O_4$ /rGO
% Degradation	12.73	28.08	40.0	50.37
Rate constant (min^{-1})	0.0019	0.0531	0.0897	0.0112
R^2	0.8002	0.9291	0.9567	0.8557
Adj. R^2	0.7780	0.9212	0.9519	0.8397

The compared to FP and CC plans was calculated. $ZnFe_2O_4$, $Ni_{0.1}Cu_{0.1}Zn_{0.8}Fe_2O_4$, Tb-$Ni_{0.1}Cu_{0.1}Zn_{0.8}Fe_2O_4$, and Tb- $Ni_{0.1}Cu_{0.1}Zn_{0.8}Fe_2O_4$ /rGO photocatalysts were used to evaluate the photocatalytic degradation of pendimethalin Fig. 10. Fig. 11c makes it evident that Tb-$Ni_{0.1}Cu_{0.1}Zn_{0.8}Fe_2O_4$/rGO has a higher degrading activity than $ZnFe_2O_4$, $Ni_{0.1}Cu_{0.1}Zn_{0.8}Fe_2O_4$, and Tb-$Ni_{0.1}Cu_{0.1}Zn_{0.8}Fe_2O_4$. The $ZnFe_2O_4$, $Ni_{0.1}Cu_{0.1}Zn_{0.8}Fe_2O_4$, and Tb-$Ni_{0.1}Cu_{0.1}Zn_{0.8}Fe_2O_4$, and Tb-$Ni_{0.1}Cu_{0.1}Zn_{0.8}Fe_2O_4$/rGO photocatalysts' rate constants against pendimethalin are displayed in Fig. 11d. They were 0.00711 min^{-1}, 0.01509 min^{-1}, 0.01817 min^{-1}, and 0.0221 min^{-1}, respectively. Evidence suggests that Tb-NiCuZnFe_2O_4/rGO photodegraded pendimethalin more fast than other artificial photocatalysts. The percentage of pendimethalin degradation by each of the four fabricated photocatalysts is displayed in Fig. 6c. The % degradation of pendimethalein by $ZnFe_2O_4$, $Ni_{0.1}Cu_{0.1}Zn_{0.8}Fe_2O_4$, Tb- $Ni_{0.1}Cu_{0.1}Zn_{0.8}Fe_2O_4$, and Tb- $Ni_{0.1}Cu_{0.1}Zn_{0.8}Fe_2O_4$ /rGO is 29.73%, 52.99%, 56.62% and 69.50% respectively. The Tb-NiCuZnFe_2O_4/rGO demonstrated good photodegradation ability, as evidenced by the 69.50% elimination of pendimethalin in 50 minutes (Table 4).

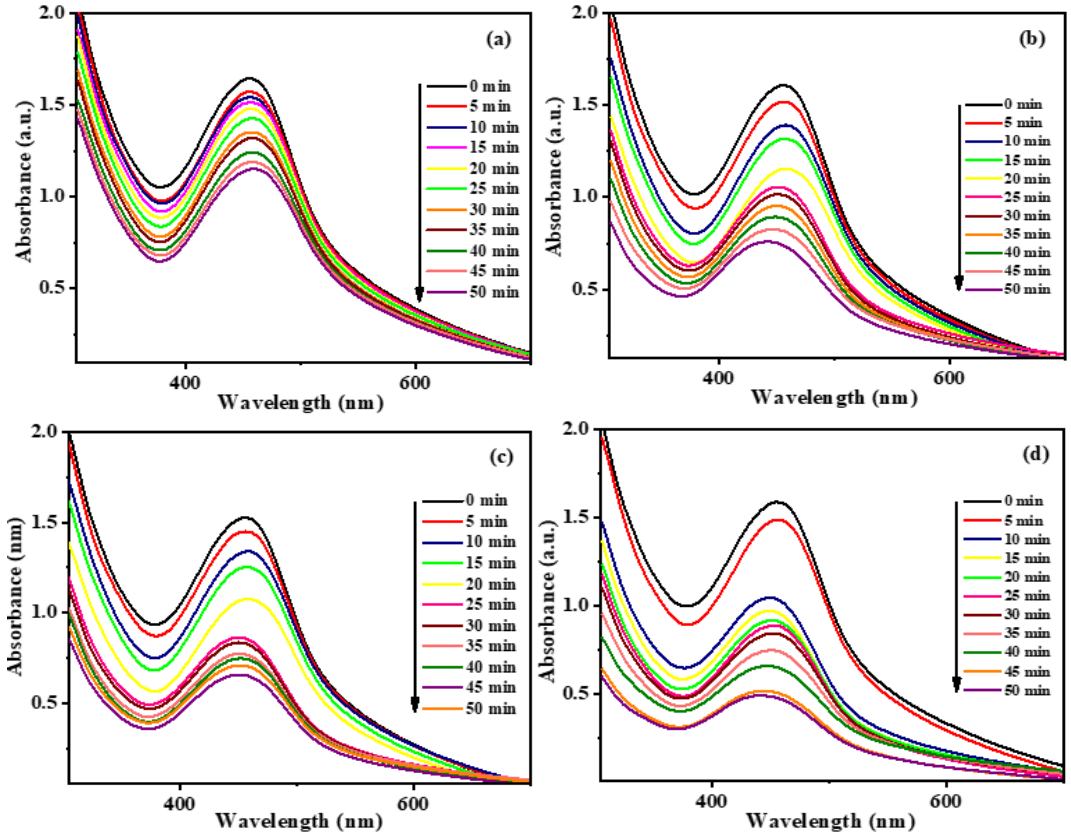

Fig. 10. Absorption spectra of Pendimethalin using (a) $ZnFe_2O_4$, (b) $Ni_{0.1}Cu_{0.1}Zn_{0.8}Fe_2O_4$, (c) Tb-$Ni_{0.1}Cu_{0.1}Zn_{0.8}Fe_2O_4$, and (d) Tb- $Ni_{0.1}Cu_{0.1}Zn_{0.8}Fe_2O_4$/rGO nanocomposite.

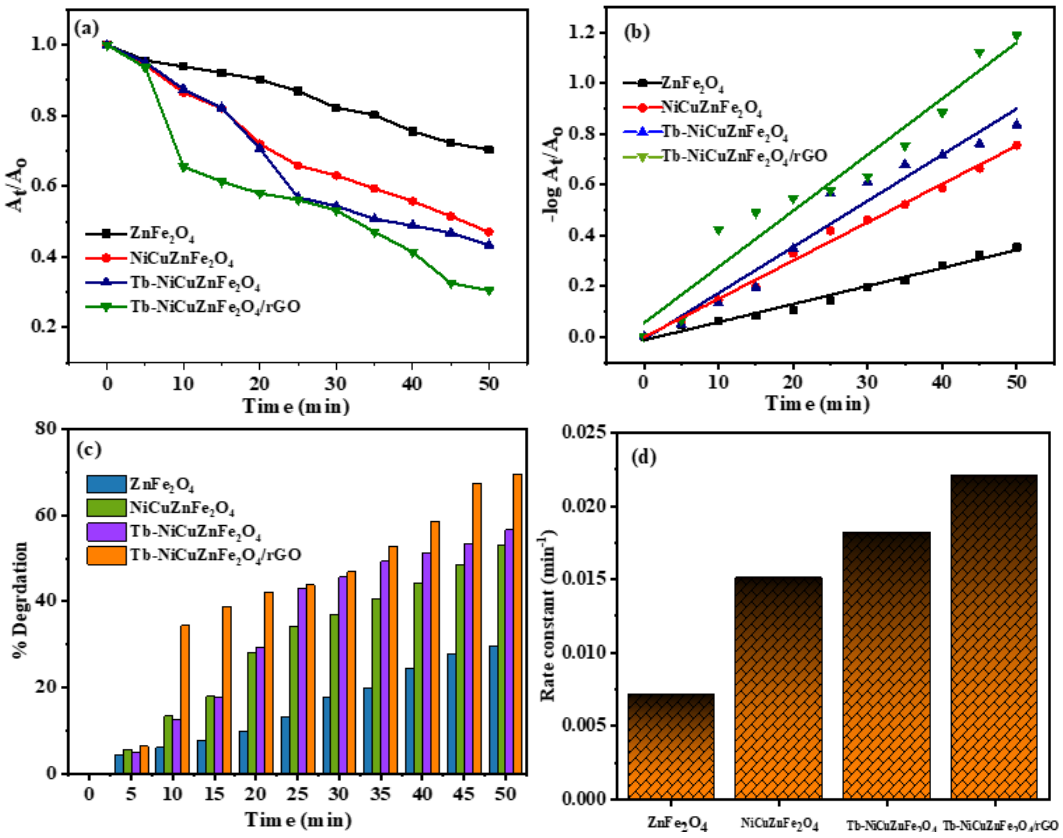

Fig. 11. (a, b) Kinetic graphs, (c) percentage degradation, and (d) rate constants of pendimethalin using $ZnFe_2O_4$, $Ni_{0.1}Cu_{0.1}Zn_{0.8}Fe_2O_4$, Tb- $Ni_{0.1}Cu_{0.1}Zn_{0.8}Fe_2O_4$ and Tb-$Ni_{0.1}Cu_{0.1}Zn_{0.8}Fe_2O_4$/rGO nanocomposites.

Table 4. Kinetic characteristics of the photocatalysts' degradation of Pendimethalin pesticide.

Sample	$ZnFe_2O_4$	$Ni_{0.1}Cu_{0.1}Zn_{0.8}Fe_2O_4$	Tb-$Ni_{0.1}Cu_{0.1}Zn_{0.8}Fe_2O_4$	Tb-$Ni_{0.1}Cu_{0.1}Zn_{0.8}Fe_2O_4$ /rGO
% Degradation	29.73	52.99	56.62	69.50
K (min^{-1})	0.00711	0.01509	0.01817	0.0221
R^2	0.9501	0.9618	0.9932	0.9802
Adj. R^2	0.9445	0.9576	0.9924	0.9780
Half life	97.46	45.92	38.13	31.35

3.4. Scavenging experiment

The compared to FP and CC plans was calculated. A scavenging experiment was carried out to evaluate the photocatalytic mechanism and to determine and measure the contributions of different reactive species to the photodegradation of methyl orange. In this experiment, scavengers like EDTA, $AgNO_3$, 2-Propanol, and ascorbic acid were used to capture the holes (h^+), electrons (e^-), hydroxyl radicals (OH*), and superoxide radicals (O_2^{*-}), respectively (Fig. 12 and Table 4). A significant decrease in degradation activity was observed in Fig. 13 for MO dye without a scavenger in the presence of Tb-$Ni_{0.1}Cu_{0.1}Zn_{0.8}Fe_2O_4$ /rGO, indicating that photocatalytic rate decreases in the presence of these scavengers. Kinetics plots for the scavenging experiment are shown in Fig. 14(a–b) while Fig. 14(d) displayed rate constant values for 2-propanol, $AgNO_3$, EDTA, and ascorbic acid. The photocatalytic efficiency of Tb- $Ni_{0.1}Cu_{0.1}Zn_{0.8}Fe_2O_4$ /rGO nanocomposite was reduced after adding the ascorbic acid and 2-propanol, indicating that super oxide radicals (O_2^{*-}) and hydroxyl radicals OH* could affect the photodegradation rate. The addition of ascorbic acid had the greatest inhibitory effect, proving that the most active species and key players in the photocatalytic activity were (O_2^{*-}) radicals. Additionally, experimental data demonstrated that the primary species involved

in photocatalytic activity were superoxide (O_2^{*-}) and hydroxyl radicals (OH*), whereas holes contributed least to the dye solution's photodegradation. Ascorbic acid, 2-propanol, $AgNO_3$, and EDTA were found to be present in only 44.71%, 59.65%, 77.15%, and 82.30% of MO degradation cases, respectively. This demonstrates the following order of reactive species involved in MO degradation:

$$h^+ > e^- > OH^* > O_2^{*-}$$

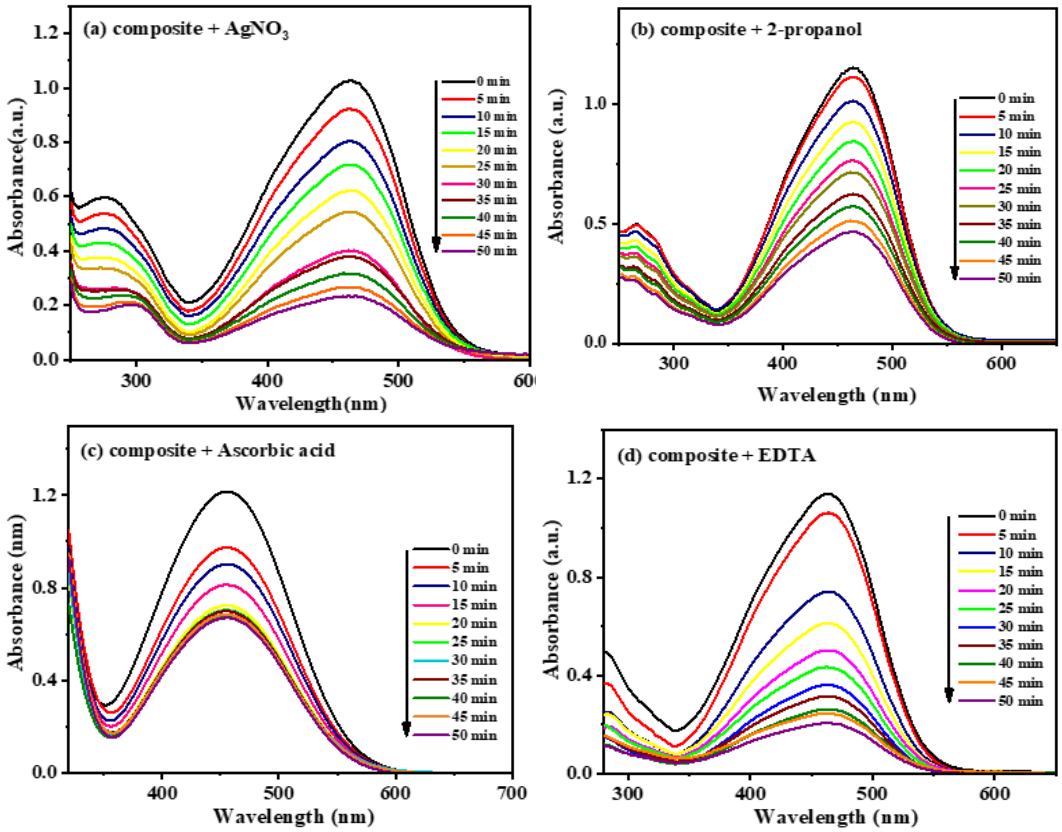

Fig. 12. Absorption spectra of dye (methyl orange) degradation using Tb- $Ni_{0.1}Cu_{0.1}Zn_{0.8}Fe_2O_4$/rGO nanocomposites with various scavengers.

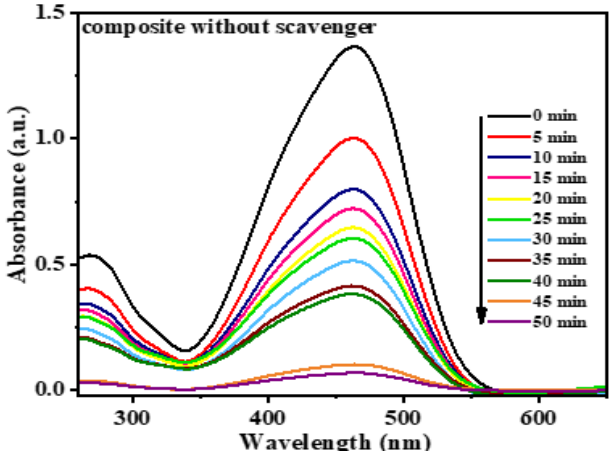

Fig. 13. Absorption spectra of MO using Tb- $Ni_{0.1}Cu_{0.1}Zn_{0.8}Fe_2O_4$/rGO nanocomposite without scavengers.

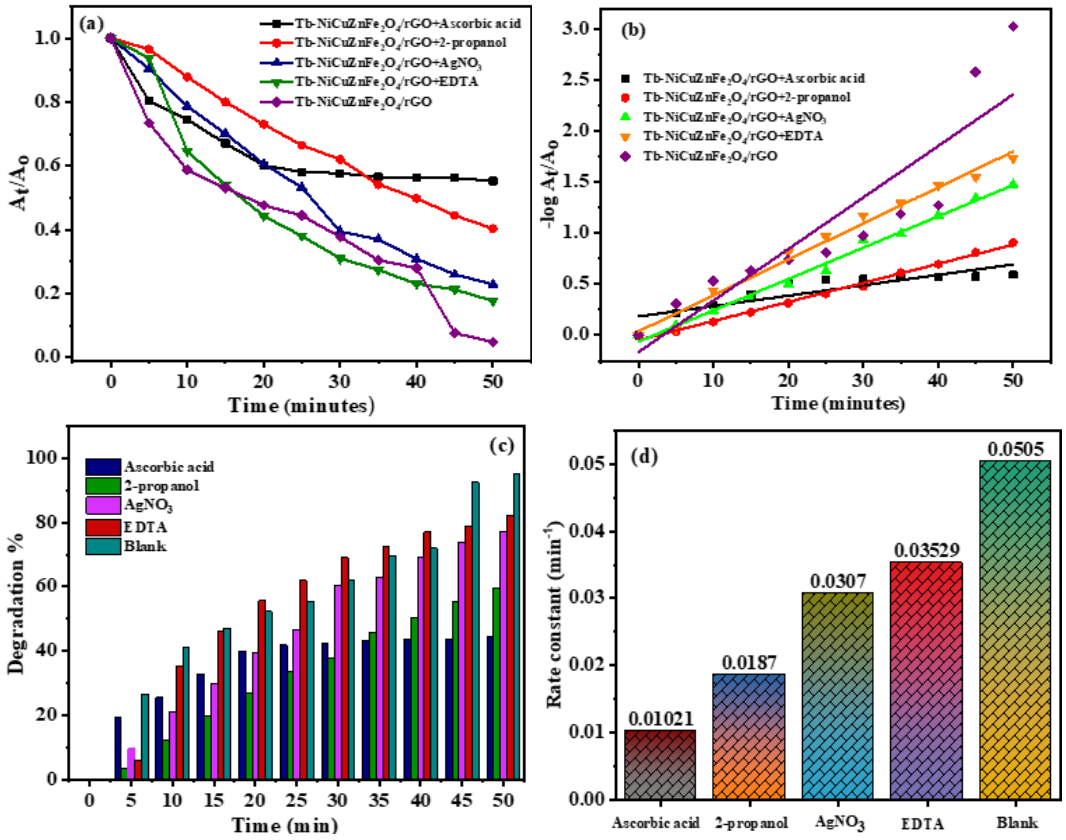

Fig. 14. Percentage degradation and kinetic graphs of MO using Tb- $Ni_{0.1}Cu_{0.1}Zn_{0.8}Fe_2O_4$ /rGO nanocomposites with and without various scavengers.

Table 4. Various kinetic factors associated with MO degradation with or without different scavengers.

Model Scavenger	Photocatalyst	% Degradation	Rate constant (min^{-1})
No Scavenger	Tb- $Ni_{0.1}Cu_{0.1}Zn_{0.8}Fe_2O_4$ /rGO	95.14	0.05
EDTA (h^+)	Tb- $Ni_{0.1}Cu_{0.1}Zn_{0.8}Fe_2O_4$ /rGO	82.30	0.04
$AgNO_3$ (e^-)	Tb- $Ni_{0.1}Cu_{0.1}Zn_{0.8}Fe_2O_4$ /rGO	77.15	0.03
2-propanol (OH*)	Tb- $Ni_{0.1}Cu_{0.1}Zn_{0.8}Fe_2O_4$ /rGO	59.65	0.02
Ascorbic acid (O_2*-)	Tb- $Ni_{0.1}Cu_{0.1}Zn_{0.8}Fe_2O_4$ /rGO	44.71	0.01

3.5. The photodegradation: a proposed reaction mechanism

The mechanism of photocatalytic degradation consists of three fundamental stages: (a) adsorption of pollutants on the surface of the photocatalyst, (b) absorption of light by the catalyst, and (c) photogeneration of electron-hole pairs . The following equation estimates the potential route of photoactive species [36]. The optical bandgap energy of a semiconductor, previously determined from the Tauc plot, is denoted by E_g, whereas the energy of a free electron, E^e, is 4.5 eV relative to NHE. Figure 15 shows the band energy alignment of Tb- $Ni_{0.1}Cu_{0.1}Zn_{0.8}Fe_2O_4$ s-NRs using equations (9) and (10). When exposed to the simulated light source, electrons in the valance band of Tb-$Ni_{0.1}Cu_{0.1}Zn_{0.8}Fe_2O_4$/rGO are driven to the conduction band due to its appropriately tiny band gap (1.82→ 1.67 eV), leaving behind positive holes. To promote charge transfer and inhibit electron-hole recombination, the electrons in the Tb- $Ni_{0.1}Cu_{0.1}Zn_{0.8}Fe_2O_4$ conduction band thermodynamically move towards rGO via highly conductive pathways supported by rGO acquaintances. This is because the conduction band of Tb- $Ni_{0.1}Cu_{0.1}Zn_{0.8}Fe_2O_4$ (E_{CB}= -0.216 eV) is located below the graphene Energy level (-0.08 eV)[37]. Additionally, the frequency of recombination processes is further decreased by the creation of an internal electric field at the S-C

interface as a result of charge transfer[38]. Due to their higher negative potential (-0.046 eV versus NHE) than O_2/O_2^{*-}, the photoexcited electrons transported to the rGO surface cause the surface oxygen to be reduced to O_2^{*-}[39]. The valence band holes in Tb- $Ni_{0.1}Cu_{0.1}Zn_{0.8}Fe_2O_4$, however, contain a positive potential (E_{VB}=1.60 eV) that is adequate to allow dyes to be directly oxidized or for H_2O and ^{-}OH to be converted to *OH . The MO dye is then degraded into CO_2 and H_2O by O_2^{*-} and *OH. An overview of these entire responses is as follows:

$$\text{Tb- } Ni_{0.1}Cu_{0.1}Zn_{0.8}Fe_2O_4/\text{rGO} + h\nu \rightarrow \text{Tb- } Ni_{0.1}Cu_{0.1}Zn_{0.8}Fe_2O_4\,(e^-_{CB}/\,h^+_{VB})\,/\text{rGO} \quad (6)$$

$$\text{Tb- } Ni_{0.1}Cu_{0.1}Zn_{0.8}Fe_2O_4\,(e^-_{CB}/\,h^+_{VB})\,/\text{rGO} \rightarrow \text{Tb- } Ni_{0.1}Cu_{0.1}Zn_{0.8}Fe_2O_4\,(h^+_{VB})\,/\text{rGO}(e^-_{CB}) \quad (7)$$

$$\text{rGO}\,(e^-_{CB}) + O_2 \rightarrow O_2^{*-} + \text{rGO} \quad (8)$$

$$O_2^{*-} + \text{Methyl orange} \rightarrow \text{Degradation Products} \quad (9)$$

$$\text{Tb-NiCuZnFe}_2O_4\,(h^+_{VB}) + H_2O/\,HO^- \rightarrow HO^* + H^+ \quad (10)$$

$$HO^* + \text{Methyl orange} \rightarrow \text{Degraded Products } (H_2O \,\&\, CO_2) \quad (11)$$

$$\text{Tb- } Ni_{0.1}Cu_{0.1}Zn_{0.8}Fe_2O_4\,(h^+_{VB}) + \text{MO} \rightarrow \text{Degraded Products } (H_2O \,\&\, CO_2) \quad (12)$$

4. Conclusion

In this work, co-precipitation method followed by ultra-sonication were used to fabricate four distinct compositions ($ZnFe_2O_4$, $Ni_{0.1}Cu_{0.1}Zn_{0.8}Fe_2O_4$, Tb- $Ni_{0.1}Cu_{0.1}Zn_{0.8}Fe_2O_4$, and Tb-$Ni_{0.1}Cu_{0.1}Zn_{0.8}Fe_2O_4$/rGO), from which Tb- $Ni_{0.1}Cu_{0.1}Zn_{0.8}Fe_2O_4$/rGO has outstanding photocatalytic activity. The optical behavior, and structure of the fabricated photocatalysts were examined using ultraviolet (UV)-visible spectroscopy and XRD, respectively. The cubic symmetry of $ZnFe_2O_4$, $Ni_{0.1}Cu_{0.1}Zn_{0.8}Fe_2O_4$, Tb-$Ni_{0.1}Cu_{0.1}Zn_{0.8}Fe_2O_4$, and Tb-$Ni_{0.1}Cu_{0.1}Zn_{0.8}Fe_2O_4$/rGO with crystallite sizes 11-15 nm was noticed. The remarkable rate of MO dye degradation demonstrated by Tb-$Ni_{0.1}Cu_{0.1}Zn_{0.8}Fe_2O_4$/rGO in experimental settings was 0.0339 min^{-1}. Under the same experimental conditions, the Tb-$Ni_{0.1}Cu_{0.1}Zn_{0.8}Fe_2O_4$/rGO photocatalyst demonstrated 83%, 69.50%, and 50.37% decolorization of MO, pendimethalin, and ofloxacin, respectively. Scavenger investigations indicated that superoxide radicals (O_2^{*-}) and hydroxyl radicals (OH*) were the primary contributors to the dye degradation pathway. The reactivation of pi-conjugated framework of Tb-$Ni_{0.1}Cu_{0.1}Zn_{0.8}Fe_2O_4$/rGO leads to improved photocatalytic performance, a higher charge density, and more effective separation between photo-excited species.

Acknowledgements

The authors express their gratitude to Princess Nourah bint Abdulrahman University Researchers Supporting Project number (PNURSP2025R26), Princess Nourah bint Abdulrahman University, Riyadh, Saudi Arabia. The authors also express their gratitude to the Deanship of Scientific Research at the Islamic University of Madinah for the support provided to the Post-Publishing Program.

Declaration of Interest Statement

All authors declare no conflict of interest.

References

[1] Singh Vig A., Rani N., Gupta A., Pandey O. P., Solar Energy 185, 469-79 (2019); https://doi.org/10.1016/j.solener.2019.04.088

[2] Adam M. S. S., Sikander S., Qamar M. T., Iqbal S., Khalil A., Taha A. M., et al., Frontiers in Chemistry 11, 1125835 (2023); https://doi.org/10.3389/fchem.2023.1125835

[3] Oliveira T. P., Rodrigues S. F., Marques G. N., Viana Costa R. C., Garçone Lopes C. G., Aranas C., et al., Catalysts2022; https://doi.org/10.3390/catal12060623

[4] Manna M., Sen S., Environmental Science and Pollution Research 30, (10), 25477-505 (2023); https://doi.org/10.1007/s11356-022-19435-0

[5] Chen X., Liu L., Yu P., Mao Y., Science (New York, NY) 331, 746-50 (2011); https://doi.org/10.1126/science.1200448

[6] Babel S., Sekartaji P. A., Sudrajat H., Environmental Science and Pollution Research 28, (24), 31163-73 (2021); https://doi.org/10.1007/s11356-021-12977-9

[7] Liu Y., Yu L., Hu Y., Guo C., Zhang F., Wen Lou X., Nanoscale 4, (1), 183-7 (2012); https://doi.org/10.1039/C1NR11114K

[8] Wei X., Wang X., Pu Y., Liu A., Chen C., Zou W., et al., Chemical Engineering Journal 420, 127719 (2021); https://doi.org/10.1016/j.cej.2020.127719

[9] Wu S., Cao H., Yin S., Liu X., Zhang X., The Journal of Physical Chemistry C 113, (41), 17893-8 (2009); https://doi.org/10.1021/jp9068762

[10] Prabhu Y. T., Navakoteswara Rao V., Shankar M. V., Sreedhar B., Pal U., New Journal of Chemistry 43, (17), 6794-805 (2019); https://doi.org/10.1039/C8NJ06056H

[11] Nguyen L. T., Nguyen H. T., Le T. H., Nguyen L. T., Nguyen H. Q., Pham T. T., et al., Materials 14, (8), 2054 (2021); https://doi.org/10.3390/ma14082054

[12] Zakir R., Iqbal S. S., Rehman A. U., Nosheen S., Ahmad T. S., Ehsan N., et al., Ceramics International 47, (20), 28575-83 (2021); https://doi.org/10.1016/j.ceramint.2021.07.016

[13] Siao Y.-J., Qi X., Journal of Alloys and Compounds 691, 672-82 (2017); https://doi.org/10.1016/j.jallcom.2016.08.316

[14] Szytuła A., Leciejewicz J., Handbook of Crystal Structures and Magnetic Properties of Rare Earth Intermetallics2020; https://doi.org/10.1201/9780138719411

[15] Kabbur S. M., Waghmare S. D., Nadargi D. Y., Sartale S. D., Kambale R. C., Ghodake U. R., et al., Journal of Magnetism and Magnetic Materials 473, 99-108 (2019); https://doi.org/10.1016/j.jmmm.2018.10.041

[16] Dhiman P., Rana G., Alshgari R. A., Kumar A., Sharma G., Naushad M., et al., Environmental Research 216, 114665 (2023); https://doi.org/10.1016/j.envres.2022.114665

[17] Rosales-González O., Bolarín-Miró A. M., Cortés-Escobedo C. A., Pedro-García F., Patiño-Pineda J. A., Sánchez-De Jesús F., Ceramics International 49, (4), 6006-14 (2023); https://doi.org/10.1016/j.ceramint.2022.10.101

[18] Jasrotia R., Suman, Verma A., Verma R., Godara S. K., Ahmed J., et al., Ceramics International 48, (19, Part B), 29111-20 (2022); https://doi.org/10.1016/j.ceramint.2022.05.050

[19] Munir M. A., Naz M. Y., Shukrullah S., Farooq M. U., Kamran K., Irfan M., et al., Materials Science and Engineering: B 291, 116374 (2023); https://doi.org/10.1016/j.mseb.2023.116374

[20] Patil B. B., Pawar A. D., Bhosale D. B., Ghodake J. S., Thorat J. B., Shinde T. J., Journal of Nanostructure in Chemistry 9, (2), 119-28 (2019); https://doi.org/10.1007/s40097-019-0302-0

[21] Awati V., Badave K., Bobade D., Indian Journal of Physics 96, (1), 89-101 (2022); https://doi.org/10.1007/s12648-020-01955-5

[22] Almessiere M. A., Slimani Y., Unal B., Zubar T. I., Sadaqat A., Trukhanov A. V., et al., Journal of Materials Research and Technology 9, (5), 10608-23 (2020); https://doi.org/10.1016/j.jmrt.2020.07.094

[23] Asif R. M., Aziz A., Akhtar M. N., Amjad M., Khan M. A., Physica B: Condensed Matter 653, 414658 (2023); https://doi.org/10.1016/j.physb.2023.414658

[24] Jamdade S. G., Tambade P. S., Rathod S. M., Matematika 14, (2), 254-63 (2023); https://doi.org/10.17586/2220-8054-2023-14-2-254-263

[25] Chen Y., Wu Q., Bu N., Wang J., Song Y., Chemical Engineering Journal 373, 192-202 (2019); https://doi.org/10.1016/j.cej.2019.05.047

[26] Habte A. T., Ayele D. W., Advances in Materials Science and Engineering 2019, 5058163 (2019); https://doi.org/10.1155/2019/5058163

[27] Imae I., Coatings 11, (3), 297 (2021); https://doi.org/10.3390/coatings11030297

[28] Murtaza A., Basha B., Farooq Warsi M., Alrowaili Z. A., Al-Buriahi M. S., Munir S., Materials Science and Engineering: B 294, 116532 (2023); https://doi.org/10.1016/j.mseb.2023.116532

[29] Basha B., Ikram M., Alrowaili Z. A., Al-Buriahi M. S., Anwar M., Suleman M., Ceramics International, (2023).

[30] Bashir S., Jamil A., Khan M., Alazmi A., Abuilaiwi F., Shahid M., Journal of Alloys and Compounds 913, 165214 (2022); https://doi.org/10.1016/j.jallcom.2022.165214

[31] Baig M. M., Zulfiqar S., Yousuf M. A., Shakir I., Aboud M. F. A., Warsi M. F., Journal of Hazardous Materials 402, 123526 (2021); https://doi.org/10.1016/j.jhazmat.2020.123526

[32] Ansari M. R., Peta K. R., Recent Advances in Nanomaterials. Singapore: Springer Nature Singapore; 2024. p. 49-55; https://doi.org/10.1007/978-981-99-4878-9_7

[33] Rahman A., Aadil M., Akhtar M., Warsi M. F., Jamil A., Shakir I., et al., Ceramics International 46, (9), 13517-26 (2020); https://doi.org/10.1016/j.ceramint.2020.02.136

[34] Dhiman P., Dhiman N., Kumar A., Sharma G., Naushad M., Ghfar A. A., Journal of Molecular Liquids 294, 111574 (2019); https://doi.org/10.1016/j.molliq.2019.111574

[35] Lü X.-f., Ma H.-r., Zhang Q., Du K., Research on Chemical Intermediates 39, (9), 4189-203 (2013); https://doi.org/10.1007/s11164-012-0935-9

[36] Mousavi M., Habibi-Yangjeh A., Abitorabi M., Journal of colloid and interface science 480, 218-31 (2016); https://doi.org/10.1016/j.jcis.2016.07.021

[37] Su T., Shao Q., Qin Z., Guo Z., Wu Z., ACS Catalysis 8, (3), 2253-76 (2018); https://doi.org/10.1021/acscatal.7b03437

[38] Aruljothi C., Manivel P., Vasuki T., Carbon Letters 32, (7), 1703-14 (2022); https://doi.org/10.1007/s42823-022-00372-4

[39] Chaudhary K., Shaheen N., Zulfiqar S., Sarwar M. I., Suleman M., Agboola P. O., et al., Synthetic Metals 269, 116526 (2020); https://doi.org/10.1016/j.synthmet.2020.116526